AIAA 2005-3543

Stability of Rockets with Headwall Injection

E. M. Abu-Irshaid and J. Majdalani
Advanced Theoretical Research Center
University of Tennessee Space Institute
Tullahoma, TN 37388

G. Casalis
ONERA-CERT
31055 Toulouse Cedex 4, France

41st AIAA/ASME/SAE/ASEE Joint Propulsion Conference and Exhibit
10–13 July 2005
Tucson, AZ

41st AIAA/ASME/SAE/ASEE Joint Propulsion Conference and Exhibit
10-13 July 2005, Tucson, Arizona

AIAA 2005-3543

Stability of Rockets with Headwall Injection

Esam M. Abu-Irshaid* and Joseph Majdalani†
University of Tennessee Space Institute, Tullahoma, TN 37388

and

Grégoire Casalis‡
ONERA-CERT, 2 Avenue Ed. Belin, B.P. 4025, 31055 Toulouse Cedex 4, France

We investigate the hydrodynamic instability of the full-length, cylindrical models of solid and hybrid rockets with headwall injection. Our baseline is the rotational incompressible flowfield proposed in a recent study (Majdalani, J. and Vyas, A. B., "Inviscid Models of the Classic Hybrid Rocket," AIAA Paper 2004-3474). The local non-parallel approach (LNP) is implemented in which the amplitude functions are assumed to be radially dependent at fixed streamwise locations. The usual singularity along the chamber axis is eliminated using Taylor series expansions. As a result, three compatibility relations are derived and substituted for the local boundary conditions along the axis. These depend on whether the tangential wave number q is 0, 1 or larger. Our rotational model is shown to exhibit a range of instability that broadens with successive increases in headwall injection. The lowest frequency below which the flow remains unconditionally stable is observed at ω = 28.5 regardless of the headwall injection rate. As usual, the zeroth order tangential mode is found to be the most amplified. Using a representative headwall injection velocity for hybrid rockets, we identify a range of frequencies along which large excursions in pressure and velocity amplitudes are possible. These surges signal the presence of a resonant-like mechanism that is akin to an acoustic instability response. The most excited frequencies vary between 387 and 415 in the vicinity of the headwall. These frequencies are spatially delayed and lowered to 93.8-163.5 when the headwall injection rate is reduced to the level associated with solid rockets. For the most critical streamwise stations, these resurging wave amplitudes are quantified and shown to exhibit spectra that mimic the waterfall data acquired in acoustic instability tests.

Nomenclature

a	=	chamber radius
l	=	chamber aspect ratio, L/a
P	=	normalized pressure, $\bar{P}/(\rho U_w^2)$
p	=	normalized pressure fluctuation, $\bar{p}/(\rho U_w^2)$
Re	=	injection Reynolds number, $U_w a/\nu$
r, z	=	normalized radial or streamwise coordinate, $\bar{r}/a$, $\bar{z}/a$
u	=	normalized velocity fluctuation, $(\bar{u}_r, \bar{u}_z, \bar{u}_\theta)/U_w$
U_0	=	maximum headwall injection velocity, $\bar{U}_{\bar{z}}(0,0)$
U_w	=	maximum sidewall injection velocity, $-\bar{U}_r(a,\bar{z})$
u_0	=	normalized headwall injection velocity, U_0/U_w
u_h	=	headwall injection constant, $U_0/(\pi U_w)$ or $U_0/(2U_w)$
U	=	normalized mean inflow velocity, $(\bar{U}_r, \bar{U}_z)/U_w$

*Graduate student and Research Associate, Department of Mechanical, Aerospace and Biomedical Engineering. Member AIAA.
†Jack D. Whitfield Professor of High Speed Flows, Department of Mechanical, Aerospace and Biomedical Engineering. Member AIAA.
‡Research Scientist, Aerodynamics and Energetics Modeling Department. Member AIAA.

μ = dynamic viscosity
ν = kinematic viscosity, μ/ρ
ρ = density

Subscripts
i = inlet property
h = property at the headwall
w = property at the sidewall
r = radial component or partial derivative
z = axial component or partial derivative
θ = azimuthal/tangential component or partial derivative
$\bar{M}$ = overbars denote dimensional variables
$\tilde{M}$ = denotes total (instantaneous) quantities
$\hat{m}$ = denotes fluctuating quantities

I. Introduction

IN this study, three-dimensional linear instability theory is applied to an idealized representation of a full-length, cylindrical, hybrid rocket. The analysis also considers a long, full-length solid rocket motor (SRM) with reactive headwall. The Local Non Parallel (LNP) approach is used in which all of the non-zero components of the basic flow are retained in the viscous Navier-Stokes equations. In recent studies, Casalis and co-workers[1-4] have quite adroitly implemented this approach while investigating both the porous channel and tube; their mean flow expressions due to Taylor[5] and Culick[6] are often used to describe the bulk gas motion in slab and circular-port rocket motors. Their results have been corroborated by cold-flow experiments and have helped to point out the critical abscissas beyond which the flow becomes unstable.[7] These were found to occur around 5 and 3 for the planar and axisymmetric cases, respectively. This investigation follows suit by applying the LNP approach to a similar geometric setting that is germane to the conventional hybrid grain shape and that of a solid propellant motor with reactive headend. Here the headwall is made permeable to permit the imposition of an inlet profile that observes Berman's similarity equation.[8]

The first numerical study of hydrodynamic instability in an SRM model was carried out by Varapaev and Yagodkin.[9] An extended investigation that included laboratory measurements and full solutions of the Navier-Stokes equations was performed by Casalis and co-workers;[1,3] this helped to explain the effects of radial disturbances and the inconsistencies between the two available techniques, namely, those that relied on perturbing either the primitive variables or the streamfunction.[10,11] In similar context, the purpose of this work is to explore the hydrodynamic instability of the idealized solid and hybrid rockets. This will be accomplished by employing as our baseline the core flow of the cylindrical rocket with headwall injection presented recently by Majdalani and Vyas.[12] Therein, two flowfield solutions were proposed and these will be treated using spatial instability theory. The emphasis will be largely placed on the rotational model because of the minimal value gained from the irrotational solution.

The paper is organized as follows. In the first section, we introduce the two mean flowfields and their corresponding geometry. Then we pursue the linear instability analysis based on small perturbations by normal mode decomposition. We implement the numerical procedure while paying particular attention to the indivisible treatment of singularity along the axis. In fact, the treatment of singularity enables us to derive the remaining boundary conditions needed to achieve closure. Next, the algorithm is verified by ensuring its ability to reproduce the same stability information for an SRM with non-reactive headwall. The corresponding flowfield is often referred to as Culick's[6] (or Taylor's[5]) and happens to be an important special case of the rotational hybrid model for which the headwall injection velocity is set to zero. After gaining confidence in the proposed methodology, results for the solid and hybrid models are presented and discussed.

II. Geometry and Mean Flow Equations

A. Geometry

As mentioned above, two hybrid core flow models are explored, specifically, rotational and irrotational. In both models (see Fig. 1) the motor is represented as a cylindrical chamber of length L and radius a. In the rotational case, the headwall injection velocity is assumed to be Berman's cosine function with a maximum centerline velocity

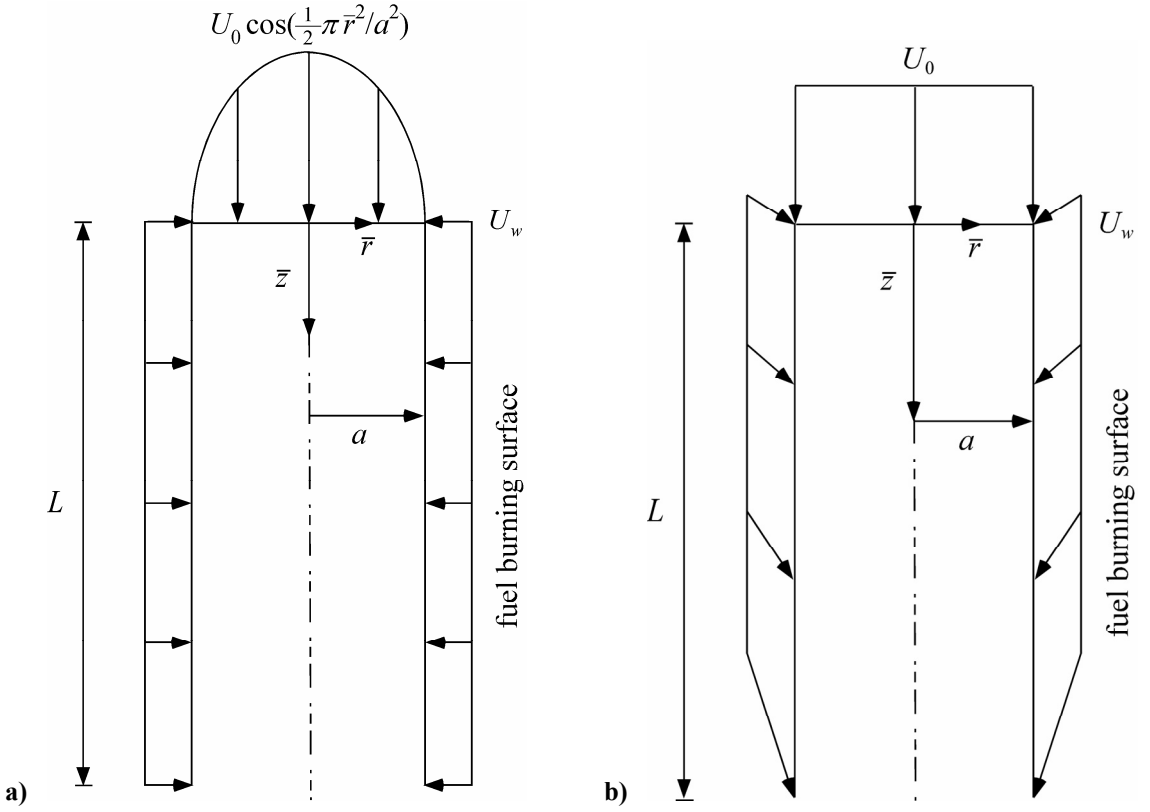

Figure 1. In a) we sketch the rotational full-length rocket model permitting mass addition along both sidewall and headwall boundaries. In b) the irrotational model is presented for which uniform mass injection is applied at the headwall while slip is allowed along the sidewall.

equal to U_0. This velocity can be adjusted to reproduce the rate of mass addition at the injector faceplate of a hybrid rocket. On the other hand, the independent sidewall injection U_w is used to capture the regression rate of the solid fuel (Fig. 1a). The simpler, irrotational model shown in Fig. 1b assumes a constant headwall injection velocity equal to U_0 with radial sidewall injection equal to U_w; in the latter case, however, the no-slip condition at the sidewall is sacrificed. As indicated in the Nomenclature, all coordinates are normalized by the chamber radius and velocities are normalized by U_w. In particular, the headwall injection constant is defined as $U_0/(\pi U_w)$ and $U_0/(2U_w)$ for the rotational and irrotational cases, respectively. Note that $z=0$ stands for the upstream edge of the porous wall. The corresponding mean flow components are given by[12]

$$\begin{cases} U_r = -\sin(\frac{1}{2}\pi r^2)/r \\ U_z = \pi(z+u_h)\cos(\frac{1}{2}\pi r^2) \ \text{(rotational)} \\ U_\theta = 0 \end{cases} \tag{1}$$

and

$$\begin{cases} U_r = -r \\ U_z = 2(z+u_h) \ \text{(irrotational)} \\ U_\theta = 0 \end{cases} \tag{2}$$

Before engaging the attendant analysis, it may be useful to recall that the headwall injection constant germane to hybrid rockets falls in the range of $50 \le u_h \le 500$.[12] At present, we start with $u_h = 0$ for the purpose of providing a benchmark that can be compared to existing solutions developed for SRMs with impervious headwalls.[2] Another

rotational case that is worth considering is $u_h = \frac{1}{2}$; this ratio ensures that the headwall rate of mass addition is equal to $\rho\pi a^2 U_w$, hence consistent with that of a sufficiently long solid propellant grain burning equally uniformly along its headwall and sidewall.

B. Governing Equations

In this problem, three-dimensional incompressible flow is treated using cylindrical coordinates; the normalized Navier-Stokes and the continuity equations are written as:

continuity equation

$$\frac{\partial \tilde{U}_r}{\partial r} + \frac{\tilde{U}_r}{r} + \frac{1}{r}\frac{\partial \tilde{U}_\theta}{\partial \theta} + \frac{\partial \tilde{U}_z}{\partial z} = 0 \tag{3}$$

r-momentum equation

$$\frac{\partial \tilde{U}_r}{\partial t} + \tilde{U}_r \frac{\partial \tilde{U}_r}{\partial r} + \frac{\tilde{U}_\theta}{r}\frac{\partial \tilde{U}_r}{\partial \theta} - \frac{\tilde{U}_\theta^{\,2}}{r} + \tilde{U}_z \frac{\partial \tilde{U}_r}{\partial z} + \frac{\partial \tilde{P}}{\partial r}$$

$$= \frac{1}{Re}\left[\frac{\partial^2 \tilde{U}_r}{\partial r^2} + \frac{1}{r}\frac{\partial \tilde{U}_r}{\partial r} - \frac{\tilde{U}_r}{r^2} + \frac{1}{r^2}\frac{\partial^2 \tilde{U}_r}{\partial \theta^2} - \frac{2}{r^2}\frac{\partial \tilde{U}_\theta}{\partial \theta} + \frac{\partial^2 \tilde{U}_r}{\partial z^2}\right] \tag{4}$$

θ-momentum equation

$$\frac{\partial \tilde{U}_\theta}{\partial t} + \tilde{U}_r \frac{\partial \tilde{U}_\theta}{\partial r} + \frac{\tilde{U}_\theta}{r}\frac{\partial \tilde{U}_\theta}{\partial \theta} + \frac{\tilde{U}_r \tilde{U}_\theta}{r} + \tilde{U}_z \frac{\partial \tilde{U}_\theta}{\partial z} + \frac{1}{r}\frac{\partial \tilde{P}}{\partial \theta} = \frac{1}{Re}\left[\frac{\partial^2 \tilde{U}_\theta}{\partial r^2} + \frac{1}{r}\frac{\partial \tilde{U}_\theta}{\partial r} - \frac{\tilde{U}_\theta}{r^2} + \frac{1}{r^2}\frac{\partial^2 \tilde{U}_\theta}{\partial \theta^2} + \frac{2}{r^2}\frac{\partial \tilde{U}_r}{\partial \theta} + \frac{\partial^2 \tilde{U}_\theta}{\partial z^2}\right] \tag{5}$$

z-momentum equation

$$\frac{\partial \tilde{U}_z}{\partial t} + \tilde{U}_r \frac{\partial \tilde{U}_z}{\partial r} + \frac{\tilde{U}_\theta}{r}\frac{\partial \tilde{U}_z}{\partial \theta} + \tilde{U}_z \frac{\partial \tilde{U}_z}{\partial z} + \frac{\partial \tilde{P}}{\partial z} = \frac{1}{Re}\left[\frac{\partial^2 \tilde{U}_z}{\partial r^2} + \frac{1}{r}\frac{\partial \tilde{U}_z}{\partial r} + \frac{1}{r^2}\frac{\partial^2 \tilde{U}_z}{\partial \theta^2} + \frac{\partial^2 \tilde{U}_z}{\partial z^2}\right] \tag{6}$$

where r, θ, z are dimensionless coordinates.

C. Linear Instability Theory

The linear instability principle consists of introducing a small sinusoidal disturbance into the Navier-Stokes equations in order to compute the range of unstable frequencies. A small perturbation $\hat{m}$ is hereby superimposed on the mean flowfield in each of its principal variables M. Assuming a total solution of the form $\tilde{M} = M + \hat{m}$, the small disturbances can be synthesized using normal mode decomposition vis-à-vis

$$\begin{cases} \hat{u}_r = u_r(r)\exp\left[i(q\theta + \alpha z - \omega t)\right] \\ \hat{u}_\theta = u_\theta(r)\exp\left[i(q\theta + \alpha z - \omega t)\right] \\ \hat{u}_z = u_z(r)\exp\left[i(q\theta + \alpha z - \omega t)\right] \\ \hat{p} = p(r)\exp\left[i(q\theta + \alpha z - \omega t)\right] \end{cases} \tag{7}$$

where q is the tangential (i.e., azimuthal) wave number. Note that the complex amplitudes are only dependent on r. In the general case α and ω are complex and can be expressed by

$$\alpha = \alpha_r + i\alpha_i \text{ and } \omega = \omega_r + i\omega_i \tag{8}$$

Here α_r is the longitudinal wave number and ω_r is the circular frequency. While $-\alpha_i$ represents the growth rate in space, ω_i denotes the growth rate in time. Using the temporal disturbance argument, the flow is allowed to grow with time when $\alpha_i = 0$. Conversely, the spatial disturbance argument permits the flow to grow in space when $\omega_i = 0$. According to available experimental evidence, it may be argued that the spatial theory is more suitable to treat this problem. At the outset, $\omega_r/(2\pi)$ will provide the dimensionless frequency of the disturbances.

Equations (3)–(6) can be perturbed using $\tilde{U} = U + \hat{u}$ and $\tilde{p} = P + \hat{p}$. The resulting set is then expressible as function of the disturbance amplitudes by substitution of the normal mode transformations given by Eq. (7). After some algebra, one finds

$$\frac{\mathrm{d}u_r}{\mathrm{d}r} + \frac{u_r}{r} + iq\frac{u_\theta}{r} + i\alpha u_z = 0 \tag{9}$$

$$-i\omega u_r + U_r\frac{\mathrm{d}u_r}{\mathrm{d}r} + u_r\frac{\mathrm{d}U_r}{\mathrm{d}r} + i\alpha U_z u_r + \frac{\mathrm{d}p}{\mathrm{d}r} = \frac{1}{Re}\left(\frac{\mathrm{d}^2u_r}{\mathrm{d}r^2} + \frac{1}{r}\frac{\mathrm{d}u_r}{\mathrm{d}r} - \frac{u_r}{r^2} - \frac{q}{r^2}u_r - \frac{2}{r^2}iqu_\theta - \alpha^2 u_r\right) \tag{10}$$

$$-i\omega u_\theta + U_r\frac{\mathrm{d}u_\theta}{\mathrm{d}\theta} + \frac{U_r u_\theta}{r} + i\alpha U_z u_\theta + \frac{iq}{r}p = \frac{1}{Re}\left(\frac{\mathrm{d}^2u_\theta}{\mathrm{d}r^2} + \frac{1}{r}\frac{\mathrm{d}u_\theta}{\mathrm{d}r} - \frac{u_\theta}{r^2} - \frac{q^2}{r^2}u_\theta + \frac{2}{r^2}iqu_r - \alpha^2 u_\theta\right) \tag{11}$$

$$-i\omega u_z + U_r\frac{\mathrm{d}u_z}{\mathrm{d}z} + u_r\frac{\mathrm{d}U_z}{\mathrm{d}r} + i\alpha U_z u_z + \frac{\mathrm{d}U_z}{\mathrm{d}z}u_z + i\alpha p = \frac{1}{Re}\left(\frac{\mathrm{d}^2u_z}{\mathrm{d}r^2} - \frac{1}{r}\frac{\mathrm{d}u_z}{\mathrm{d}r} - \frac{q}{r^2}u_z - \alpha^2 u_z\right) \tag{12}$$

This system encapsulates the interactions between mean components of velocity and the unsteady disturbances $\boldsymbol{u}(r)$ and $p(r)$. The implicit assumption is that while the steady (U_r, U_z) prescribe the motion and growth of unsteady waves, they themselves remain indifferent to the oscillations that they engender. In a recent study by Venugopal,[13] it was shown that fluctuations are highly sensitive to the mean flow distribution, particularly, along the axis. This reiterates the need to use the most suitable mean flow model for a given application. It also justifies the quest for refined mean flow models of rocket chambers. In what follows, a careful set of boundary conditions is presented and discussed.

D. Vital Boundary Conditions

Equations (9)–(12) are second order in u_r, u_θ and u_z; upon close examination, it may be determined that the total order is equal to six when $q \neq 0$ and reduces to four when $q = 0$ (see Section E). Of the required boundary conditions, three may be inferred from the velocity adherence condition at the sidewall. As no slip is observed at leading order by the mean flow ingredient, the fluctuations must vanish at the sidewall to avoid local interference. This implies

$$u_r = u_\theta = u_z = 0 \text{ at } r = 1 \tag{13}$$

Three conditions are missing still. To compensate, we expand the principal variables and substitute them into the linearised Navier-Stokes system. Suppression of singular terms will then be used to extract the three desired constraints. Thus, using a polynomial expansion for the fluctuations,

$$u_r = \sum_{n=0}^{\infty} v_n r^n, \quad u_\theta = \sum_{n=0}^{\infty} w_n r^n, \quad u_z = \sum_{n=0}^{\infty} u_n r^n, \quad p = \sum_{n=0}^{\infty} p_n r^n \tag{14}$$

and, similarly, for the steady field,

$$U_z = f(z)\sum_{n=0}^{\infty} A_n r^n, \quad U_r = \sum_{n=0}^{\infty} B_n r^n, \quad U_\theta = 0 \tag{15}$$

these series may be substituted into Eqs. (9)–(12) and rearranged. Forthwith, singularities of order r^{-1} and r^{-2} are identified and collected in the mass conservation and radial momentum equations. To ensure a uniformly valid outcome, these terms are eliminated. The remaining parts appear at $O(1)$ and $O(r^n)$. We find the $O(1)$ member in continuity to be useful and, as such, we classify it along the r^{-2} system of equations. At length, we gather

System 1

$$\begin{cases} v_0 + iqw_0 = 0 \\ (1+q^2)v_0 + 2iqw_0 = 0 \\ 2iqv_0 - w_0(1+q^2) = 0 \\ -q^2 u_0 = 0 \end{cases} \quad (r^{-1} \text{ members}) \tag{16}$$

System 2

$$\begin{cases} 2v_1 + iqw_1 = -i\alpha u_0 \ \text{ from continuity at } O(1) \\ -q^2 v_1 - 2iqw_1 = 0 \\ 2iqv_1 - q^2 w_1 = Re\left(iqp_0 + w_0 B_0\right) \\ u_1(1-q^2) = 0 \end{cases} \quad (r^{-2} \text{ members}) \tag{17}$$

At this juncture, the radial momentum equation is transformed into a gigantic system of equations that can be resolved to any order of accuracy depending on the summation integer n. This set is given by

System 3 (r^n members, $n \geq 0$)

$$(n+3)v_{(n+2)} + iqw_{(n+2)} + i\alpha u_{(n+1)} = 0 \tag{18}$$

$$\left[(n+2)^2 - (1+q^2)\right]v_{(n+2)} - 2iqw_{(n+2)} - Re(n+1)p_{(n+1)}$$

$$= Re\left\{\left(\frac{\alpha^2}{Re} - i\omega\right)v_n + \sum_{j=0}^{n}\left[(i\alpha fA_j + (j+1)B_{(j+1)})v_{(n-j)} + (n-j+1)B_j v_{(n-j+1)}\right]\right\} \tag{19}$$

$$2iqv_{(n+2)} + ((n+2)^2 - (1+q^2))w_{(n+2)} - B_0 w_{(n+1)} - iqRep_{(n+1)}$$

$$= Re\left\{\left(\frac{\alpha^2}{Re} - i\omega\right)w_n + \sum_{j=0}^{n}\left[(B_{(j+1)} + i\alpha fA_j + (n-j+1)w_{(n-j+1)}\right]\right\} \tag{20}$$

$$\left[(n+2)^2 - q^2\right]u_{(n+2)} - (\alpha^2 - iRe\omega)u_n - i\alpha Rep_n$$

$$= Re\sum_{i=1}^{n}\left\{\left[(f' + i\alpha f)A_j\right]u_{(n+1)} + (n-j+1)u_{(n-j+1)}B_{(j)} + f(j+1)A_{(j+1)}v_{(n-j)}\right\} \tag{21}$$

System 1 can be readily expressed in terms of velocity fluctuations. Depending on the tangential wave number, one can put, along the centerline,

$$\begin{cases} q = 0 \rightarrow u_r(0) = u_\theta(0) = \dfrac{\mathrm{d}u_z}{\mathrm{d}r}(0) = 0 \\ q = 1 \rightarrow \dfrac{\mathrm{d}u_r}{\mathrm{d}r}(0) = \dfrac{\mathrm{d}u_\theta}{\mathrm{d}r}(0) = u_z(0) = 0 \\ q \geq 2 \rightarrow u_r(0) = u_\theta(0) = u_z(0) = 0 \end{cases} \tag{22}$$

The three original boundary conditions due to no slip may now be supplemented by Eq. (22) to provide a complete set of auxiliary conditions for the velocity. To secure the pressure at $q = 0$, one can substitute the findings in Eq. (22) back into the $r-$momentum expression in Eq. (10) (or, equivalently, by utilizing the first three equations of System 2). This enables us to deduce that $p'(0) = 0$. However, for $q \geq 1$, the first three equations of System 2 can be solved to obtain, along the centerline, the trivial set corresponding to $v_1 = w_1 = 0$ and $p_0 \equiv p(0) = 0$. We are thus compelled to apply a normalization condition for the pressure at the sidewall that does not affect the solution. Without loss in generality, we therefore set $p(1) = 1$. By so doing, the pressure magnitude becomes a normalizing factor for all remaining amplitudes.

E. The Shooting Procedure

Equations (9)–(12) can be rearranged and manipulated into six first-order ODEs. Our approach follows precisely that of Malik.[23] Thus u_r' is taken from mass conservation and inserted into the *r*-momentum equation. The latter is reduced to a first-order ODE with two boundary conditions. The extra condition is used to secure convergence at the opposing boundary (here, we choose the sidewall as our shooting target). The six ODEs that must be solved form a linear set that can be expressed as

$$\frac{\mathrm{d}Z_i}{\mathrm{d}r} = [\mathbf{C}]\, Z_j, i = 1,2,\ldots,6\ ;\ [\mathbf{Z}] = \left\{ u_r, u_\theta, \frac{\mathrm{d}u_\theta}{\mathrm{d}r}, u_z, \frac{\mathrm{d}u_z}{\mathrm{d}r}, p \right\}^T \tag{23}$$

The coefficient matrix $[\mathbf{C}]$ is prescribed by

$$[\mathbf{C}] = \begin{pmatrix} C_{11} & C_{12} & 0 & C_{14} & 0 & 0 \\ 0 & C_{21} & 0 & 0 & 0 & 0 \\ C_{31} & C_{32} & C_{33} & 0 & 0 & 0 \\ 0 & 0 & 0 & C_{45} & 0 & 0 \\ C_{51} & 0 & 0 & C_{54} & C_{55} & C_{56} \\ C_{61} & C_{62} & C_{63} & C_{64} & C_{65} & 0 \end{pmatrix}; \quad \begin{cases} C_{11} = -\dfrac{1}{r}\ ,\ C_{12} = -\dfrac{iq}{r}\ ,\ C_{14} = -i\alpha,\ C_{21} = 1 \\ C_{31} = -\dfrac{2iq}{r^2} \\ C_{32} = Re\left(-i\omega + \dfrac{U_r}{r} + i\alpha U_z \right) + \dfrac{1}{r^2}\left(q^2+1\right) + \alpha^2 \\ C_{33} = ReU_r - \dfrac{1}{r}\ ,\ C_{36} = Re\dfrac{iq}{r} \end{cases} \tag{24}$$

and

$$\begin{cases} C_{31} = -\dfrac{2iq}{r^2},\ C_{32} = Re\left(-i\omega + \dfrac{U_r}{r} + i\alpha U_z \right) + \dfrac{1}{r^2}\left(q^2+1\right) + \alpha^2 \\ C_{33} = ReU_r - \dfrac{1}{r},\ C_{36} = Re\dfrac{iq}{r},\ C_{45} = 1,\ C_{55} = ReU_r - \dfrac{1}{r},\ C_{56} = Re\dfrac{iq}{r} \\ C_{51} = ReU_z',\ C_{54} = Re\left(-i\omega + i\alpha U_z + \dfrac{\partial U_z}{\partial z} \right) + \dfrac{q^2}{r^2} + \alpha^2,\ C_{64} = i\alpha U_r,\ C_{65} = \dfrac{1}{Re}\left(-i\alpha\right) \\ C_{61} = \dfrac{1}{Re}\left(-\dfrac{q^2}{r^2} - \alpha^2 \right) + i\omega + \dfrac{U_r}{r} - U_r' - i\alpha U_z,\ C_{62} = \dfrac{1}{Re}\left(-\dfrac{iq}{r^2} \right) + U_r\dfrac{iq}{r},\ C_{63} = \dfrac{1}{Re}\left(-\dfrac{iq}{r} \right) \end{cases} \tag{25}$$

This system admits a non-trivial solution by virtue of the pressure condition being non-homogeneous. In order to expedite convergence, we find it instructive to discretize all terms in Z_i' using Chebyshev's spectral collocation method.[14] At present, 200 collocation points are used in conjunction with Muller's root solving algorithm; these are found to be sufficient to ensure the desired tolerance set at 10^{-9} in α. This is further explained in the companion paper that addresses the stability of the bidirectional vortex.[15] In marching forward, our dispersion relation linking all primitive variables and parameters takes the form of $f(\alpha, \omega, q, z, Re, u_h) = 0$. Thus, in order to make headway, we choose for each tangential wave number q a certain frequency $\omega \equiv \omega_r$ at a fixed set of operating parameters (Reynolds number and headwall injection constant u_h). We then iterate at every spatial position of interest z on the complex α until the target velocity amplitude u_r is made to vanish at the sidewall. This yields the amplitude vector $[\mathbf{Z}]$ in addition to the spatial growth rate $-\alpha_i$, and the wave number α_r. From α_r, one may calculate the

spatial wavelength, $\lambda = 2\pi/\alpha_r$ and the axial speed of propagation (or phase velocity), $\dot{x} = \omega/\alpha_r$. After determining our first two α_r values, we linearly extrapolate for the subsequent initial guess. Throughout this simulation, we fix the Reynolds number at 5,000 and u_h for the application at hand. At this high level of sidewall injection, it is universally accepted that inviscid conditions will prevail to the extent that our steady-state model becomes an accurate representation of the incompressible core flow. We therefore assume that the physical model satisfies the fundamental criteria for which compressibility may be ignored. These are extensively described in the companion paper by Majdalani.[16]

The second parameter that is left invariant for a given simulation is the tangential wave number q. Thus, for each frequency ω, we march in space up to the point prescribed by $z = 20$. The axial extent is covered in equal spatial increments of 0.1. After completing each sweep, we then increase the frequency by a variable amount: at low ω, we use a fine step size of 1 to capture the critical frequency at the nose-tip of the iso-*n* curves; these are defined and illustrated in the next section. The step size is then increased to 5 and 10 as we approach linear behavior in the iso-*n* curves. The maximum frequency we explore depends on the headwall injection constant. For $u_h = 0.5$, our maximum frequency reaches 175 whereas for $u_h = 50$ we find it necessary to raise the bar to 800. The highest ω that we investigate is the one that enables us to capture the most amplified value of n at $z = 15$. This typically coincides with the iso-*n* curve reaching an amplification factor of $n = 11$. Based on existing experimental data with no headwall injection, transition to turbulence takes place between $n = 7$ and 9 according to stability theory[2] and experiments.[17] For $u_h = 0.5$, a similar behavior is expected. It can thus be argued that any evolution beyond $n = 9$ may no longer observe linear instability theory or help to delimit the unstable domain. More experimental work with headwall injection is therefore required to substantiate further refinement to this analysis.

III. Results and Discussion

A verification of the numerical procedure used to solve Eq. (23) subject to Eq. (22) can be carried out by applying our algorithm to the special case of $u_h = 0$. Results are illustrated in Table 1 and these are compared to published data.[4] Note the favorable agreement between the current code and that used by Griffond and Casalis.[4] Solutions are matching in five-to-ten significant digits. Using the same algorithm, we have carried out the analysis of the irrotational model described by Eq. (2); we report that the results inhibit any type of amplification using both temporal and spatial techniques. In the interest of brevity, these results are excluded.

From a practical standpoint, we recognize that the effect of the headwall injection constant u_h must be carefully investigated alongside the effect of varying the tangential wave number. The graph for the iso-*n* factor is first computed for four cases involving $u_h = 0.5$, $Re = 5,000$, and $q = 0,1,2,3$; these cases represent the first four tangential fluctuation modes of an SRM with headwall burning (see Fig. 2). The iso-*n* factors represent the spatial amplification of the flow and can be computed from fixed values of $Re, q, z,$ and ω. The amplitude of the wave A is calculated by integrating the local amplification growth rate ($-\alpha_i$) as described in Eq. (26): the value of $z_0(\omega)$, the first axial position where marginal stability is reached, depends on these fixed values via

$$A(z,\omega) = A_0 e^n \quad \text{with } n(z,\omega) = -\int_{z_0(\omega)}^{z} \alpha_i(\xi,\omega)\,\mathrm{d}\xi \tag{26}$$

Here A_0 represents the last stable amplitude along the neutral curve prescribed by $n = 0$. The iso-*n* graph in Fig. 2 does not provide the necessary information needed to determine the spatial position at which the flow starts to amplify. However, other useful features can be identified based on this graph.

First, one may recognize the unstable region to be enclosed within the classic L-shaped boundary. The vertical range of unstable frequencies increases in the streamwise direction. By the same token, for each specific frequency above the horizontal branch of the curve, the *n*-factor increases as the flow approaches the downstream end of the chamber. Second, the axial position of the most amplified frequency seems to change very gradually with successive increases in q. Only a minor shift in the neutral curve is detected. Third, flow stability at a spatial position seems to increase at higher wave numbers as a result of the curves shifting in the positive z direction. This point can be seen more clearly

Table 1 Eigenvalues of the Culick profile at $\omega = 80$, $z = 10$, $q = 0$ and $Re = 4,500$

	published data[4]		present solution	
Mode	α_r	α_i	α_r	α_i
1	6.0952945656	–1.0787998140	6.0952945724	–1.0787998101
2	3.3264285366	–0.1095525589	3.3264285380	–0.1095525581
3	2.6013223310	0.1322870315	2.6013223554	0.1322830025

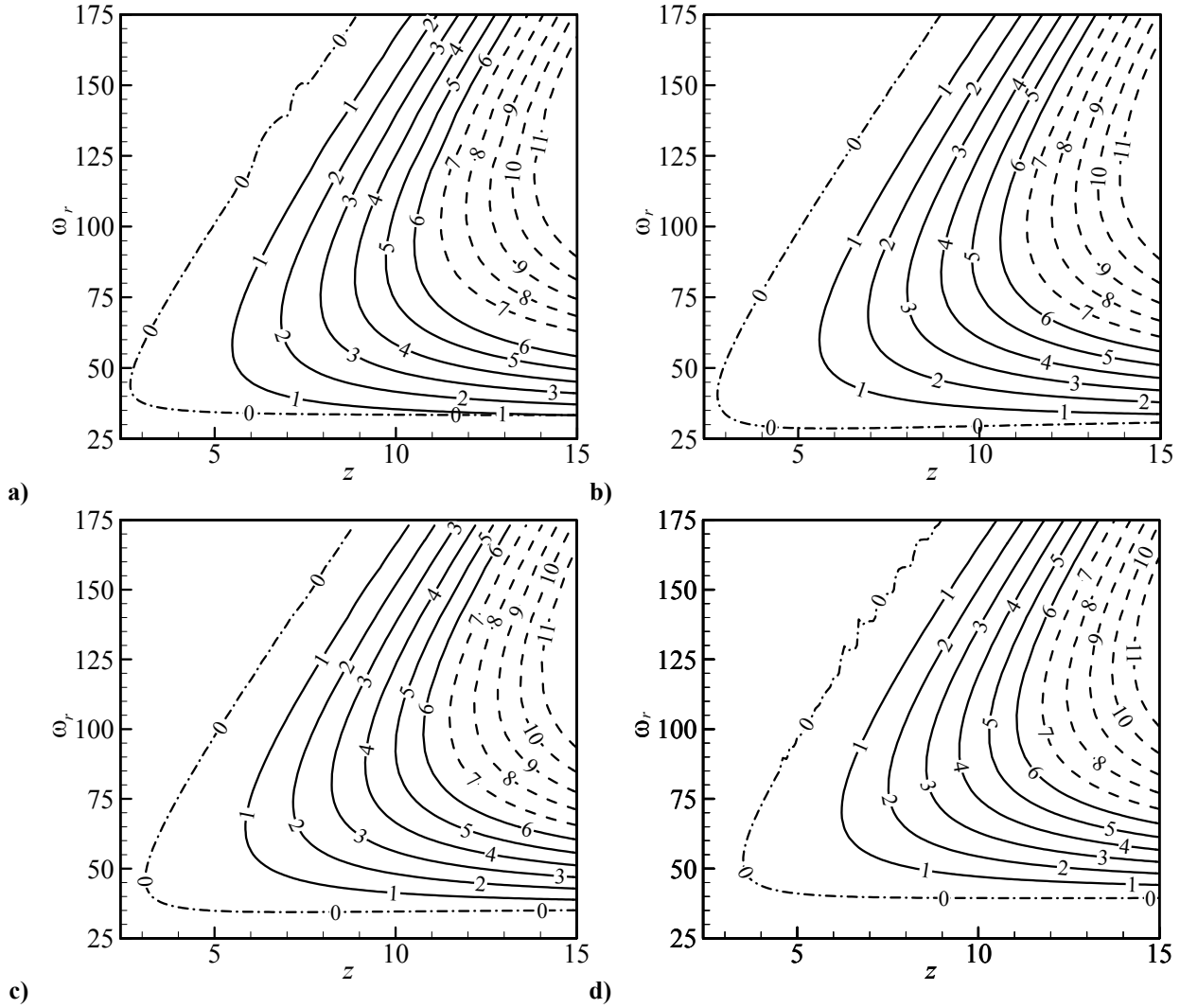

Figure 2. Iso-*n* factors for *Re* = 5,000 and u_h = 0.5. Results are shown in a) through d) for *q* = 0, 1, 2 and 3.

by comparing the neutral curves at several tangential wave numbers.

Figure 3 displays the neutral curves of Fig. 2 for $q = 0,1,2$ and 3. These represent the lines along which the flow begins to destabilize. It can be seen that the largest unstable frequency at a given z is nearly the same at all tangential wave modes. This can be attributed to the overlapping of the upper branch of the neutral curves past $z = 6$. For a sufficiently high frequency, the neutral curves at different wave numbers begin to overlap to the extent of becoming nearly imperceptible; this duplicitous behavior is confounding to the extent of making it difficult to isolate modes at a given frequency during experimental measurements.[2,17] On the other hand, due the continual spatial shifting of the lower branch in the streamwise direction (as the wave number is increased), the $q = 0$ case appears to be the most amplified. In fact, the two lowest modes, $q = 0,1$, are nearly indiscernible; this trend can make them difficult to decipher from experimental measurements.

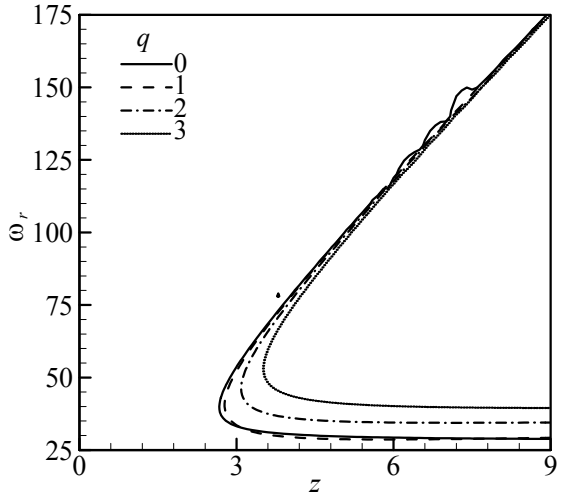

Figure 3. Neutral curves for different values of *q* at *Re* = 5,000 and u_h = 0.5.

Note that a double shooting technique has been developed to specifically calculate the lines along which both α_i and ω_i vanish simultaneously. This approach serves a dual purpose. First, it enables us to directly and expeditiously locate the neutral points, thus obviating the need to sweep horizontally across the domain to tag each of the neutral points individually. Second, as a consequence to the first, a larger number of points can be collected in a shorter period of time. This improves our resolution by permitting the use of finer increments and, thereby, deduce smoother curves.

Another observation that can be made based on Fig. 3 is that the flow is always stable below a certain frequency; in that respect, each neutral curve shows a tip that depends on the fixed parameters, $Re, q,$ and u_h. For example, in the most dominant cases of $q = 0$ and 1, the flow is always stable below a threshold frequency of $\omega_r = 28.5$; the critical values (i.e., the tips of the neutral curves) are captured at $z \simeq 2.6$ and 2.7 with a common $\omega_r = 43$ and $\alpha_r \simeq 6.40$ and 6.23, respectively. For $q = 2$, the frequency above which instability starts increases to $\omega_r = 34$; this occurs at $\omega_r = 47$, $z \simeq 3$ and $\alpha_r \simeq 6.67$. Similar trends depicting an upward shift in frequency is reported with further increases in the wave number. This behavior confirms the $q = 0$ case as being the most critical.

To examine the effect of the injection headwall constant, neutral curves for different values of u_h are processed and plotted in Fig. 4a. Clearly, as u_h increases, the flow becomes gradually more unstable; the corresponding neutral curves steadily shift upstream. The critical value, in this case, starts at the headwall injection point when the injection constant reaches $u_h \simeq 3.168$.

When $u_h > 3.168$, there will exist a range of frequencies for which the flow becomes unstable starting at the injection point itself, $z = 0$; the spectrum of frequencies widens with further departures from $u_h = 3.168$. One should point out that the critical value of u_h varies with the tangential wave number. However, the $q = 0$ case shown here remains the most critical.

As the headwall-to-sidewall injection ratio becomes large (see Fig. 4b), the flow streamlines start to resemble those of a circular-port hybrid rocket chamber.[12] By way of illustration, two values of u_h, $(10, 50)$, are selected. Here too, the range of unstable frequencies is seen to expand significantly at higher headend injection rates. It may be helpful to mention that the lowest frequency, where the flow starts to amplify (i.e., the frequency where the

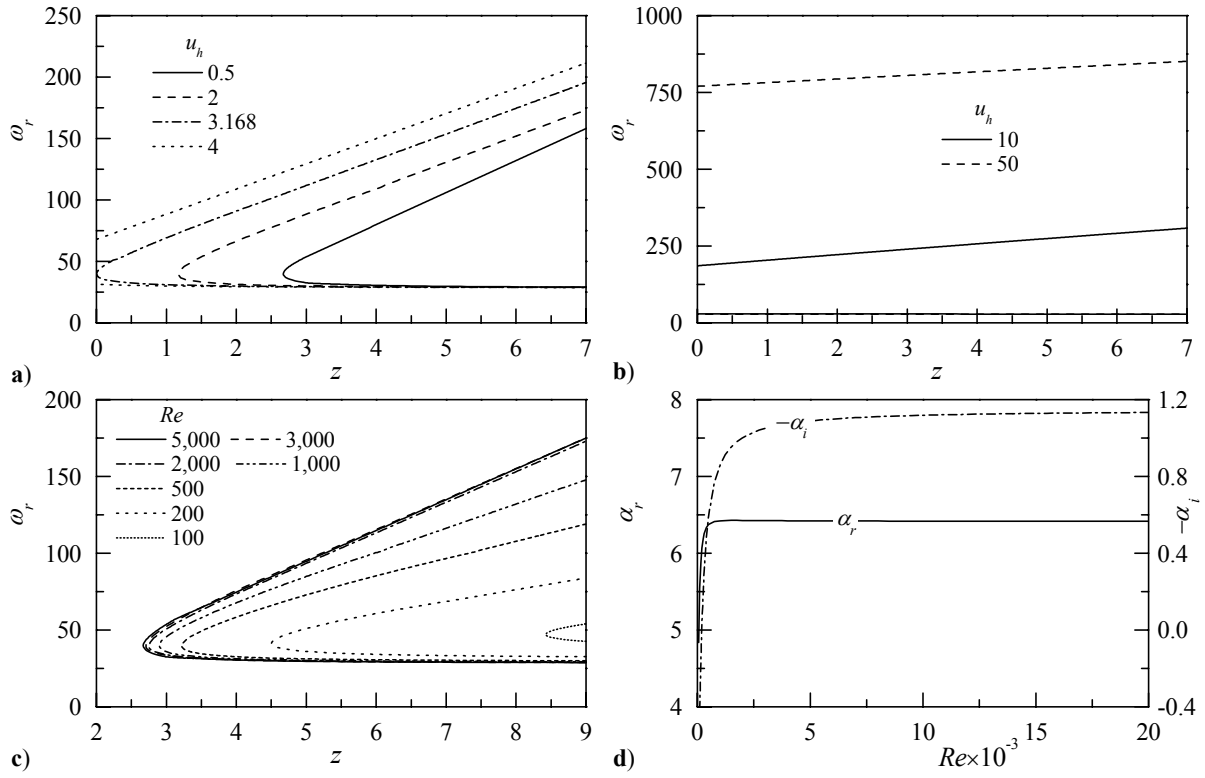

Figure 4. Using *Re* = 5,000 and *q* =0, we present the neutral curves for a) simulated SRM with headwall burning, and b) simulated hybrid rocket engine; in c) the effect of Reynolds number on the spatial shift in stability is illustrated for a simulated SRM with headwall burning (q = 0 and u_h = 0.5); for the same case, the behavior of the streamwise wave number is plotted in d) over a wide range of Reynolds numbers and fixed values of ω = 80 and z = 9.

lower, horizontal segment of the neutral curve starts to swerve) is weakly sensitive to u_h (see Fig. 4a). In contrast, the tip location and the highest unstable frequency are strongly affected by u_h. The tip moves upstream and the highest frequency increases as u_h is augmented. Additionally, as illustrated previously in Fig. 3, these features are dependent on the tangential wave number q. The impact of u_h on controlling the tip and the upper branch of the neutral curve is clearly seen in Fig. 4b; accordingly, the flow regains stability at $\omega_r \geq (185, 770)$ for $u_h = (10, 50)$, respectively.

Another interesting behavior that can be captured is the effect of Reynolds number on motor stability. To that end, Fig. 4c is used to illustrate the effect of Re on the position and size of the neutral curve. These determine the first abscissa at which instability can be experienced and the range of amplified frequencies, respectively. For $Re \geq 2,000$, a clustering in the neutral curves can be seen; this weak sensitivity to the Reynolds number marks the beginning of inviscid behavior.

As shown in Fig. 4d, the longitudinal wave number and the amplification rate $(\alpha_r, -\alpha_i)$ become independent of Re above a certain threshold value, namely, one that is often termed the critical Reynolds number, Re_c. Essentially, both α_r and $-\alpha_i$ reach their asymptotic values when the Reynolds number exceeds Re_c. This value represents the starting point for which inviscid behavior will prevail. For the special case shown in Fig. 4d, the critical value of Reynolds number is found to be $Re_c \simeq 2,225$. Note that the wave number tends to the inviscid limit faster than the growth rate and that the deviation in α_i is quite minute (cf. right-hand-scale). For $Re \geq 5,000$, no change may be observed and this justifies its adoption in the present analysis.

In the process of investigating the amplitudes of disturbances at various frequencies and spatial stations, we have uncovered an acoustic instability-like phenomenon, namely, one with potentially serious implications. We have identified the presence of rising amplitudes over a short range of frequencies for the hybrid rocket model at the zeroth tangential mode. This is illustrated in Fig. 5 where the spectrum of wave amplitudes is shown both in waterfall and planar format. We remind the reader that the amplitudes here depend on the wall pressure being set equal to unity. In Fig. 5a, the increasing pressure rises are displayed at discrete axial positions over a wide range of frequencies. The same curves are overlaid in Fig. 5b to help in tracking their relative evolution with respect to both frequencies and abscissas. Interestingly, these peaks coincide with the points where $-\alpha_i$ is largest. From the design standpoint, the frequencies that are accompanied by intense surges in pressure and velocity amplitudes constitute the most detrimental and, thereby, undesirable group. As shown on the graph, the most excited frequencies are detected between $\omega = 387$ and 415 at $z = (2, 4)$, near the headwall. Spatially, their peaks are seen to slowly drift downstream while their oscillatory amplitudes are generally diminishing. Being capable of exceeding the burst pressure of the rocket motor case, the dimensional frequencies associated with $\omega = [387 - 415]$ must be judiciously avoided in hybrid rocket design. In passing, it may be interesting to note the qualitative resemblance between Fig. 5a and experimental spectra obtained when acoustic instabilities are present in rockets. We also note that the same level of scrutiny was directed at higher tangential modes where only damped amplitudes were recovered; aside from

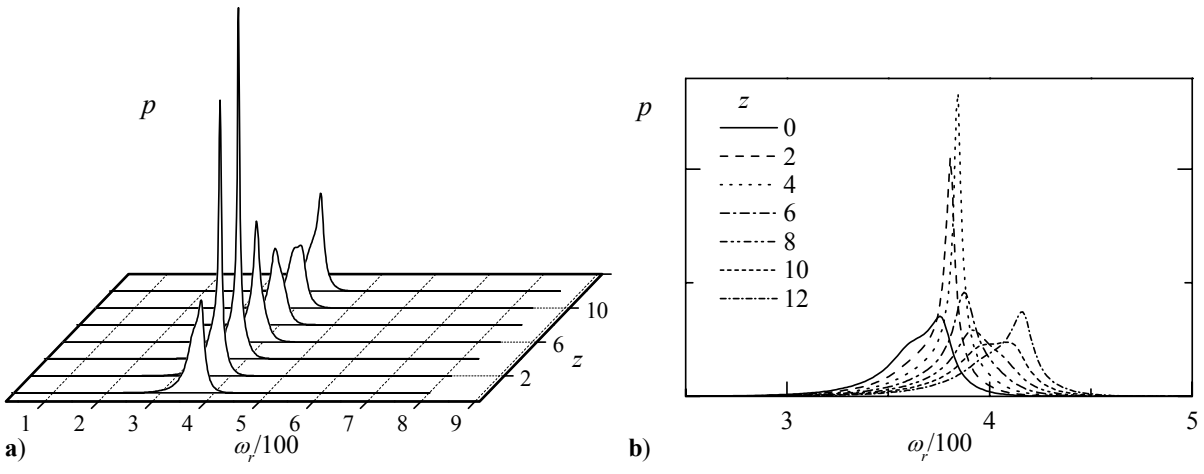

Figure 5. Spectrum of pressure amplitudes versus frequencies along a circular radius of *r* = 0.5 and increasing distance from the headwall. Note the presence of large bumps in the pressure (and similarly in the unsteady radial and streamwise velocities) over a range of undesirable frequencies. As usual, we use *Re* = 5,000 to mimic inviscid behavior, u_h = 50 for a hybrid rocket model, and *q* = 0 for the most unstable scenario.

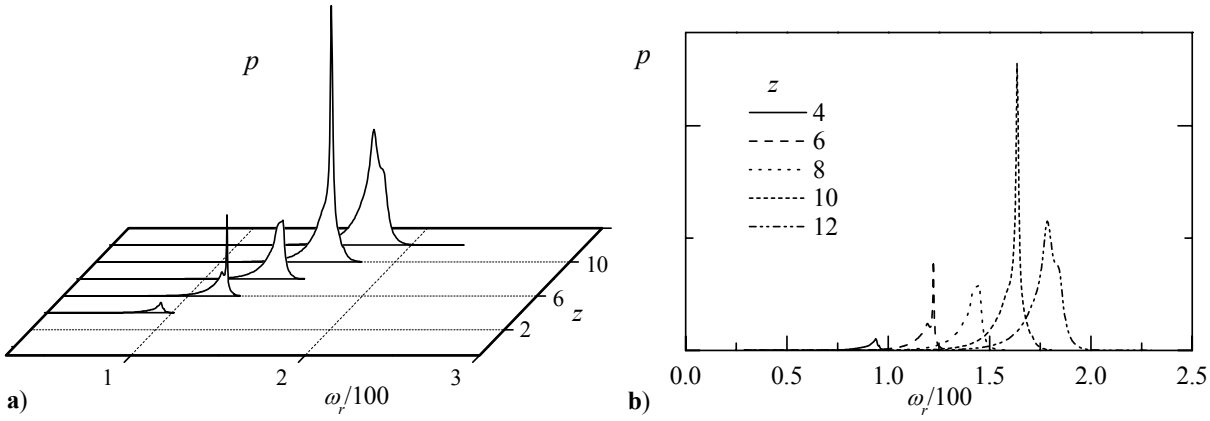

Figure 6. Same as previous except for u_h = 0.5 for a solid rocket model with reactive headwall.

$q = 0,$ no other modes were found to be susceptible to this phenomenon. When the headwall injection was reduced to $u_h = 0.5$ a similar phenomenon was observed except that the growth was spatially delayed and spread over wider and dissimilar frequency ranges (see Fig. 6). It was most pronounced near $z = 10$ and spread over a range of lower frequencies, specifically, $\omega = [93.8 - 163.5]$. The fact that the amplified frequency changes quite noticeably with z reduces the overall propensity to resonance. We thus realize that the unsafe frequencies diminish at lower headwall injection rates for which a more globally stable flowfield is obtained.

IV. Conclusions

In this article we have applied linear spatial theory to characterize the hydrodynamic instability of solid and hybrid rockets with headwall injection. We have determined that headwall injection plays a destabilizing role considering that the range of unstable frequencies is broadened with successive increases in u_h. This is also accompanied by an upstream translation of the critical abscissas and attendant shifting of the neutral curves.

By using the extended Taylor-Culick profile proposed by Majdalani and Vyas,[12] we are able to study the effect of headwall injection on stability. By using $u_h = 0.5$, our model is capable of mimicking the core flow in long solid rocket motors with reactive forward closure. Such motors are only slightly more unstable than SRMs with inert headwalls. When u_h is increased to 3.168, the most critical point along the neutral curve (i.e., the tip) is shifted upstream to the extent of reaching the headwall (by contacting the frequency axis). Thus at $z = 0$ and $\omega = 40$ the flow becomes unstable at the injection point. Further increases in u_h cause the concave portion of the neutral curve to fall behind the frequency axis, namely, in the negative z domain. Under such conditions, the flow becomes unstable even at $z = 0$ over an increasing range of frequencies. This range is bracketed by the intersection of the neutral curve and the frequency axis. The forward truncation of the neutral curve prevents us from calculating the amplification *n*-factors.

One of the most interesting aspects of this study is the discovery of a range of frequencies at the zeroth tangential mode along which enormous surges in pressure amplitudes are possible. These large excursions in pressure signal the presence of a pronounced resonant-like phenomenon that is reminiscent of an acoustic instability response. The most excited frequencies where the engine experiences the most appreciable excursions are detected in the vicinity of the headwall. These appear to slowly decrease and slowly shift away with successive decreases in headwall injection. As we march downstream we observe a quasi-steady depreciation in pressure amplitudes. From a practical standpoint, these resurging amplitudes may be the most relevant to the designer; when the amplification rates are high, they do not necessarily have a bearing on the mean pressure unless the corresponding wave amplitudes are large. It is interesting that, as the headwall injection velocity is increased, the character of the solution approaches that of parallel mean flow motion; specifically, the frequencies associated with pressure resurgences become nearly uniform, $\forall z$. This may be highly conducive to resonance by way of coupling with chamber acoustics whose frequencies are always independent of z. In future work, we plan to further investigate this phenomenon in the hope of unraveling additional connections with acoustic instability theory, especially in what regards wave amplitudes and energy accumulation rates.

Acknowledgments

The first author is sponsored by the National Science Foundation through Grant No. CMS-0353518. The second author is supported by Software and Engineering Associates (SEA), Inc., Carson City, NV. The authors thank Dr. Jonathan C. French, Senior Research Engineer, SEA, and Dr. Fred S. Blomshield, Head of Combustion and Propulsion Research, Naval Air Warfare Center, for supporting their activities in this field. Lastly, grateful appreciation is extended to Mr. François Chedevergne for commenting on this work.

References

[1]Casalis, G., Avalon, G., and Pineau, J.-P., "Spatial Instability of Planar Channel Flow with Fluid Injection through Porous Walls," *The Physics of Fluids,* Vol. 10, No. 10, 1998, pp. 2558-2568.

[2]Griffond, J., Casalis, G., and Pineau, J.-P., "Spatial Instability of Flow in a Semiinfinite Cylinder with Fluid Injection through Its Porous Walls," *European Journal of Mechanics B/Fluids,* Vol. 19, No. 1, 2000, pp. 69-87.

[3]Griffond, J., and Casalis, G., "On the Nonparallel Stability of the Injection Induced Two-Dimensional Taylor Flow," *The Physics of Fluids,* Vol. 13, No. 6, 2001, pp. 1635-1644.

[4]Griffond, J., and Casalis, G., "On the Dependence on the Formulation of Some Nonparallel Stability Approaches Applied to the Taylor Flow," *The Physics of Fluids,* Vol. 12, No. 2, 2000, pp. 466-468.

[5]Taylor, G. I., "Fluid Flow in Regions Bounded by Porous Surfaces," *Proceedings of the Royal Society, London, Series A,* Vol. 234, No. 1199, 1956, pp. 456-475.

[6]Culick, F. E. C., "Rotational Axisymmetric Mean Flow and Damping of Acoustic Waves in a Solid Propellant Rocket," *AIAA Journal,* Vol. 4, No. 8, 1966, pp. 1462-1464.

[7]Avalon, G., Casalis, G., and Griffond, J., "Flow Instabilities and Acoustic Resonance of Channels with Wall Injection," AIAA Paper 98-3218, July 1998.

[8]Berman, A. S., "Laminar Flow in Channels with Porous Walls," *Journal of Applied Physics,* Vol. 24, No. 9, 1953, pp. 1232-1235.

[9]Varapaev, V. N., and Yagodkin, V. I., "Flow Stability in a Channel with Porous Walls," *Fluid Dynamics (Izvestiya Akademii Nauk SSSR, Meckanika Zhidkosti i Gaza),* Vol. 4, No. 5, 1969, pp. 91-95.

[10]Beddini, R. A., and Roberts, T. A., "Turbularization of an Acoustic Boundary Layer on a Transpiring Surface," *AIAA Journal,* Vol. 26, No. 8, 1988, pp. 917-923.

[11]Beddini, R. A., "Injection-Induced Flows in Porous-Walled Ducts," *AIAA Journal,* Vol. 24, No. 11, 1986, pp. 1766-1773.

[12]Majdalani, J., and Vyas, A. B., "Inviscid Models of the Classic Hybrid Rocket," AIAA Paper 2004-3474, July 2004.

[13]Venugopal, P., "Direct Numerical Simulation of Turbulence in a Model Solid Rocket Motor," Ph.D. Dissertation, University of Illinois at Urbana-Champaign, 2003.

[14]Don, W. S., and Solomonoff, A., "A Boundary Value Problem with Multiple Solutions from the Theory of Laminar Flow," *SIAM Journal on Scientific Computing,* Vol. 16, No. 6, 1995, pp. 1253-1268.

[15]Abu-Irshaid, E. M., Majdalani, J., and Casalis, G., "Hydrodynamic Instability of the Bidirectional Vortex," AIAA Paper 2005-4531, July 2005.

[16]Majdalani, J., "The Compressible Taylor-Culick Flow," AIAA Paper 2005-3542, July 2005.

[17]Brown, R. S., Dunlap, R., Young, S. W., and Waugh, R. C., "Vortex Shedding as a Source of Acoustic Energy in Segmented Solid Rockets," *Journal of Spacecraft and Rockets,* Vol. 18, No. 4, 1981, pp. 312-319.